

Article



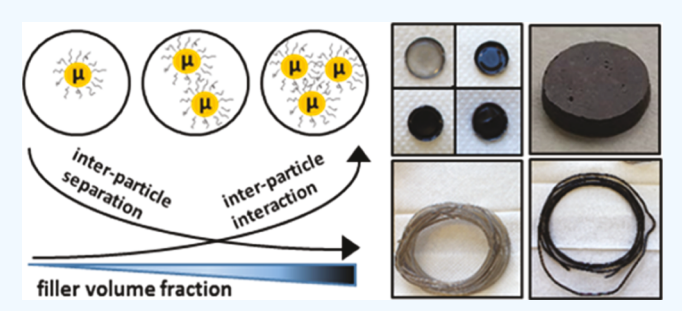
http://pubs.acs.org/journal/acsod

# Dielectric Properties for Nanocomposites Comparing Commercial and Synthetic Ni- and Fe<sub>3</sub>O<sub>4</sub>-Loaded Polystyrene

Parth N. Vakil, Faheem Muhammed, David Hardy, Tarik J. Dickens, Subramanian Ramakrishnan,\*,<sup>‡</sup> and Geoffrey F. Strouse\*,<sup>†</sup>

Supporting Information

ABSTRACT: Nanomaterial-loaded thermoplastics are attractive for applications in adaptive printing methods, as the physical properties of the printed materials are dependent on the nanomaterial type and degree of dispersion. This study compares the dispersion and the impact on the dielectric properties of two common nanoparticles, nickel and iron oxide, loaded into polystyrene. Comparisons between commercial and synthetically prepared samples indicate that well-passivated synthetically prepared nanomaterials are dispersed and minimize the impact on the dielectric properties of the host polymer by limiting particle-particle contacts.



Commercial samples were observed to phase-segregate, leading to the loss of the low-k performance of polystyrene. The change in the real and imaginary dielectric was systematically studied in two earth abundant nanoparticles at the concentration between 0 and 13 vol % (0-50 wt %). By varying the volume percentage of fillers in the matrix, it is shown that one can increase the magnetic properties of the materials while minimizing unwanted contributions to the dielectric constant and dielectric loss. The well-dispersed nanoparticle systems were successfully modeled through the Looyenga dielectric theory, thus giving one a predictive ability for the dielectric properties. The current experimental work coupled with modeling could facilitate future material choices and guide design rules for printable polymer composite systems.

# ■ INTRODUCTION

The development of printable electronics that incorporate components composed of nanoparticles embedded in polymer matrices requires a uniform nanoparticle dispersion, which will not phase-segregate under the printing conditions. The incorporation of nanoparticles (<100 nm) to modify polymer properties has been an active area of research for more than a decade.<sup>1-7</sup> Research in the early days focused on the mechanical property enhancements, although more recently, the use of nanomaterials in plastics has attracted attention for electronic applications particularly in flexible electronic applications. The dielectric properties of nanoparticle-loaded plastics can modify the dielectric properties of polymers for both high and low dielectric applications.<sup>8–13</sup> Maintaining lowk performance in polymers is critical for insulating electrical interconnects in high-density, high-speed, and high-frequency microelectronic devices, where increased resistance and capacitive coupling in the circuit lead to signal delays and electrical cross talk at interconnects. 11,14-18 Contact and noncontact printing of modified inks for two-dimensional printing<sup>19</sup> and adaptation of additive manufacturing-based fused deposition modeling (FDM)<sup>20,21</sup> using nanopolymer blends<sup>22,23,32</sup> require that the composite maintains uniform distribution of spherical nanoparticles to avoid a low percolation threshold, increase the dielectric breakdown strength and operational frequency which scales with particle loading, and have minimal impact on the polymer dielectric. 25-29 The impact on the electrical, mechanical, and optical properties of the polymer depends directly on the material type, surface passivation, and degree of dispersion.

For printed electronics, the dielectric properties of the nanocomposite are critical to maintain the low-k properties of the polymer.<sup>14</sup> Studies have shown that incorporation of uniform and small-sized nanoparticles in a dielectric insulator matrix such as a polymer can broaden the operational frequency range of the polymer dielectric, improve its dielectric breakdown strength and electromagnetic shielding capability, and improve the mechanical properties. 16-22 These studies have shown that incorporation of nano- to micron-sized particles leads to a rise in the dielectric constant with

Received: June 27, 2018 Accepted: September 26, 2018 Published: October 8, 2018



<sup>&</sup>lt;sup>†</sup>Department of Chemistry and Biochemistry, Florida State University, 95 Chieftan Way, Tallahassee, Florida 32306, United States <sup>‡</sup>Chemical & Biomedical Engineering and <sup>§</sup>Department of Industrial and Manufacturing Engineering, FAMU-FSU College of Engineering, 2525 Pottsdamer Street, Tallahassee, Florida 32310, United States

High Performance Materials Institute, 2005 Levy Avenue, Tallahassee, Florida 32310, United States

Table 1. Properties of the Nanoparticles Used (Diameter, Surface Ligand Percentage, Crystalline Structure, and Saturation Magnetization) and Nanocomposites (Choice of Nanoparticles Added and Volume Fraction of Nanoparticles)

	nanoparticles used in composites (com or syn)	NP volume fraction $\nu_{\rm f}$	NP diameter (nm) D	ligand mass %	crystalline structure	${\rm (emu/g)} \ {\rm [emu/mol} \ 10^3 {\rm ]}$
Fe <sub>3</sub> O <sub>4</sub>	(1) com	0.0137, 0.0266, 0.0935, 0.128	$16.8 \pm 5.6$	7.6	monoclinic	77.4 [17.9]
	(2) syn	0.0069, 0.0120, 0.0535, 0.109	$11.0 \pm 0.9$	28	monoclinic	58.3 [13.5]
Ni	(3) com	0.0062, 0.0129, 0.0481, 0.105	$24.0 \pm 3.3$	3.66	fcc	54.2 [3.18]
	(4) syn	0.0049, 0.0115, 0.0459, 0.0847	$23.6 \pm 3.2$	7.43	hcp	1 [0.059]

increasing particle volume fraction primarily because of phase segregation, <sup>30–35</sup> leading to interfacial polarizations at the particle—polymer interface. <sup>34,36,37</sup> Although the behavior is accounted for using effective medium theory models, the role of phase segregation is not predictable in most cases. <sup>38–44</sup>

This study investigates the use of earth abundant (cheap and widely used) nanoparticles (Ni and Fe<sub>3</sub>O<sub>4</sub>) in a known low-k dielectric polymer [polystyrene (PS)] to investigate the impact on dielectric properties of incorporating Ni and Fe<sub>3</sub>O<sub>4</sub> nanoparticles sourced from commercial (com) and synthetic (syn) methods. The nanoparticles were loaded into 280 kDa PS at increasing volume fractions and analyzed through dielectric spectroscopy, electron microscopy, small-angle Xray, and magnetic measurements to evaluate the particle distribution and dielectric properties as a function of loading level. The study demonstrates that the use of synthetically prepared nickel (Ni) and iron oxide (Fe<sub>3</sub>O<sub>4</sub>) nanoparticles of sizes under 50 nm (diameter) into PS to approximately 50% by weight outperforms commercially sourced materials. The dielectric properties of the studied nanocomposite system show that the properties can be systematically manipulated with incorporation of up to 15 vol % loading when synthetically prepared materials are employed. The composites exhibit minimal increase in permittivity and loss tangent. The frequency-dependent behavior can be modeled using effective medium theories. The use of surface-passivated nanoparticles enhanced the ability to reduce aggregation, allowing uniform blending. The composites were formed into printable filaments without inducing aggregation as evidenced by scanning electron microscopy (SEM) cross-sectional analysis. Nanoparticle composites that maintain their dispersity in the filaments are adaptable to FDM manufacturing of flexible electronics.

From an additive manufacturing outlook, the use of well-passivated, smaller nanoparticles leads to better phase dispersity in the polymer and has a lower probability of clogging print heads during FDM printing in comparison to larger-sized particles. Although nanoparticle—polymer composites using gold, silver, and high-*k* ceramics have been reported, <sup>24,45,46</sup> the use of earth abundant materials as used in this study is important if scale-up FDM printing methods are to become routine for flexible electronics. The results of the current study are believed to be extendable to other nanoparticle systems whether for optical properties (quantum dots), magnetic properties (nanomagnets), or high-*k* applications (ceramics).

## ■ RESULTS AND DISCUSSION

Using solution blending methods, com and synthetically prepared Ni and Fe<sub>3</sub>O<sub>4</sub> nanoparticles were dispersed in PS

(280 kDa) to achieve nanocomposites containing 0–15 vol % (Table 1). A volume percentage of 15% is approximately a weight percentage of 50%. Higher loadings were not studied, as the nanocomposite was observed to become brittle above 15 vol %. Because nanoparticle miscibility in PS is anticipated to be influenced by the preparative route, the nanoparticles were selected from a com and a syn source. It is important to note that the com sample is a representative sample but does not represent all possible com sources. The sourcing of the com sample was to allow quantities to be obtained at a cost comparable to syn preparative routes for the materials under study.

In Figure 1, transmission electron microscopy (TEM) of the isolated nanoparticles, size dispersity plots for the nano-

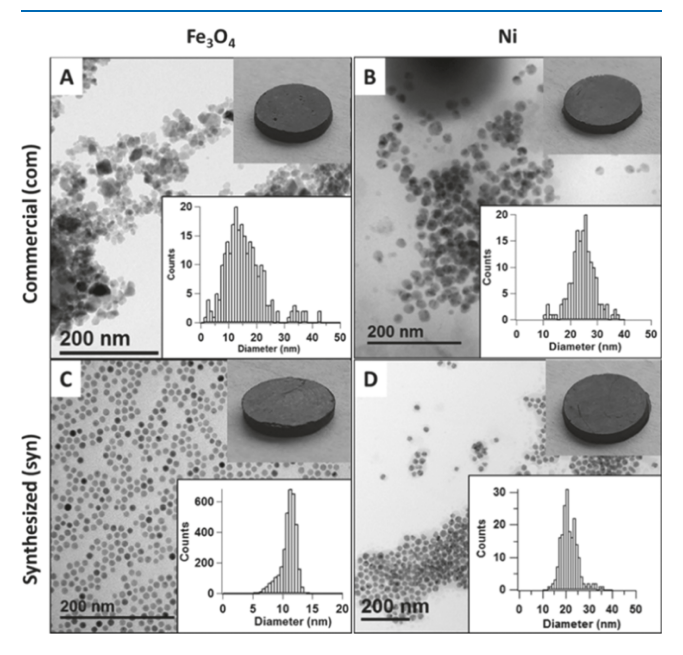


**Figure 1.** TEM size and size distribution of (A) com-Fe $_3$ O $_4$ , (B) com-Ni, (C) syn-Fe $_3$ O $_4$ , and (D) syn-Ni nanoparticles. A disk of the formed composite used in dielectric spectroscopy is shown (inset).

particles, and representative 8 mm  $\times$  1 mm nanocomposite disks are shown. Analytical data on the nanoparticles including X-ray powder diffraction, 300 K field sweep magnetization susceptibility plots, and thermogravimetric analysis (TGA) data are provided in the Supporting Information (Figures S1–S3). The studied Fe<sub>3</sub>O<sub>4</sub> nanoparticles exhibit the same crystallographic phase, but comparison of the syn and com samples reveals that the com samples are nonspherical, exhibit aggregation, and are 50% larger (3.5 times larger volume) in size with a broader size dispersity. The magnetic susceptibility

of the com sample is larger, consistent with the size difference. 47-51 The Ni nanoparticles are spherical and exhibit nearly identical size and size dispersities; however, the com sample is the strongly magnetic face-centered cubic (fcc) phase, whereas the syn sample is the weakly magnetic hexagonal close-packed (hcp) phase (Supporting Information, Figure S2). The surface passivation and ligand content are different between the four samples, as measured by TGA (Table 1). As shown in the Supporting Information (Figure S3), the ligand content from TGA measurements in syn-Fe<sub>3</sub>O<sub>4</sub> is 28.0 wt % oleic acid (OA)/oleylamine (OAm), com-Fe<sub>3</sub>O<sub>4</sub> is 7.6 wt % polyvinylpyrrolidone (PVP), syn-Ni is 7.33 wt % OAm/tri-octylphosphine (TOP), and com-Ni has <3.66 wt % ligand content (ligand is proprietary). The com variants (com-Ni and com-Fe<sub>3</sub>O<sub>4</sub>) featured a lower degree of ligand bound to the surface in comparison to the synthesized particles.

The observed PS glass-transition temperature ( $T_{\rm g}$ ) for the nanocomposites at 0 vol % and at 15 vol % nanoparticle exhibits similar  $T_{\rm g}$  values ( $T_{\rm g}=108$  °C), suggesting no impact on the polymer melting behavior (Supporting Information, Figure S4). The results are consistent with the literature on similar sized nanoparticles when dispersed in polymer matrices, where no significant change in  $T_{\rm g}$  is reported. The decomposition temperature of the nanocomposite increases with increasing particle loading as shown in the Supporting Information (Figure S5). In consistent with this result, previous studies have observed an increased thermal stability in nanoparticle-loaded polymers. S5-57

Nanoparticle Dispersion in Nanocomposites. The nanocomposites shown in Figure 1 are uniformly optically dense, exhibiting a linear increase in  $M_{\rm s}$  with increasing volume fraction (Supporting Information, Figure S2), and the powder X-ray diffraction (pXRD) shows a decrease in PS's signal intensity as the concentration of the nanoparticle increases (Supporting Information, Figure S6). The distribution of the nanoparticles in PS was analyzed using small-angle X-ray (Figure 2) and cross-sectional SEM—energy-dispersive spectroscopy (EDS) analysis (Figures 3 and 4).

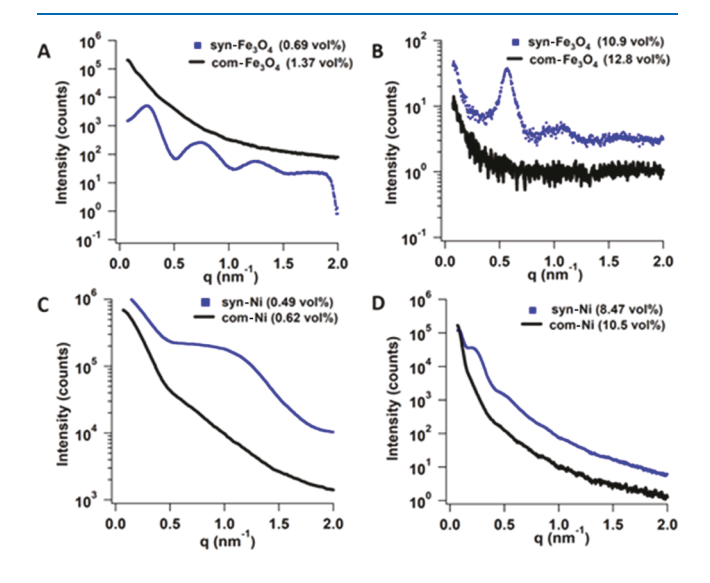


Figure 2. I vs q SAXS data for the (A) lowest loading of Fe<sub>3</sub>O<sub>4</sub> (com vs syn), (B) highest loading of Fe<sub>3</sub>O<sub>4</sub> (com vs syn), (C) lowest loading of Ni (com vs syn), and (D) highest loading of Ni (com vs syn).

Small-angle X-ray scattering (SAXS) on the highest and lowest nanoparticle loadings for both the syn and com samples were performed to investigate the microstructure of the formed composites. Of these samples, only the synthetically prepared materials could be fully analyzed. The nanocomposites formed using syn nanoparticles (Ni and Fe<sub>3</sub>O<sub>4</sub>) show a clear peak in the I versus q SAXS plot, which is indicative of ordering of particles on the length scales probed  $(2\pi/q)$ . From the SAXS data, the interparticle spacing (d) can be extracted from the length of the scattering vector q using the lowest angle primary peak  $(q^*)$  because  $d = 2\pi/q^*$ , where d = 2r + 2l (r is the nanoparticle radius and *l* represents the passivant length). In the SAXS data for syn-Fe<sub>3</sub>O<sub>4</sub> (r = 5.5 nm),  $q^*$  occurs at a q of  $0.25 \text{ nm}^{-1}$  (d = 25.1 nm) for the 0.69 vol % and a  $q^*$  of 0.565  $nm^{-1}$  (d = 11.1 nm) for the 10.9 vol %. For the syn-Ni samples (r = 12 nm), at the lowest concentration (0.49%), no definable  $q^*$  is observed in the q range probed. At high concentration (8.5 vol %), the scattering peak sharpens and occurs at 0.023  $nm^{-1}$  corresponding to d = 27 nm. The I versus q SAXS plot (Figure 2) for the com samples (Ni and Fe<sub>3</sub>O<sub>4</sub>) does not show any peaks in the scattering pattern, resulting in the inability to analyze particle distribution. Earlier studies concluded that phase segregation of the nanoparticles leads to unidentifiable scattering features. 58,59

The experimental SAXS data on the synthetically prepared systems can be interpreted in terms of the degree of dispersion in the polymer when the particle size is considered. syn-Fe<sub>3</sub>O<sub>4</sub> is 11 nm (r = 5.5 nm) with a shell of  $2l \le 5.6$  nm for the OAm [l = 1.5–2.5 nm<sup>60,61</sup>/OA (l = 2.8 nm<sup>62</sup>)] passivating shell depending on the trans to gauche content in the ligands, surface packing, and degree of passivation. If Fe<sub>3</sub>O<sub>4</sub> is aggregated, we anticipate an interparticle spacing (d) between 11 and 17 nm. 63 The SAXS data for syn-Fe<sub>3</sub>O<sub>4</sub> show at 10.9 vol %, and the interparticle spacing is consistent with a description as being aggregated within the composite. The lowconcentration (0.69 vol %) syn-Fe<sub>3</sub>O<sub>4</sub> sample can be considered on average more dispersed based on the larger interparticle distance observed in the SAXS data. For the Ni sample, the same conclusion can be made because the Ni nanoparticle would be expected to have a minimum interparticle distance of 30 nm reflecting the syn-Ni diameter 24 nm with a passivant shell of  $\leq 6$  nm (21). The measured interplanar distance of 27 nm in the SAXS data for the 10.5% Ni fits to a model where Ni is aggregated if we assume the primary peak  $(q^*)$  is observed. As the SAXS pattern arises from a combination of the form factor (particle shape and size) and structure factor (particle arrangement), calculations were performed (Supporting Information) to verify that the peak positions in the SAXS data that provide insight into the structure factor (interparticle spacing calculated previously) for the synthesized samples are not affected by the form factor. As shown in the Supporting Information (Figure S7A), the form factor for the spherical nanoparticles (taking into account the polydispersity) does not shift the peak position, validating the interparticle spacing analysis carried out earlier. On the other hand, the polydispersity of the com-Fe<sub>3</sub>O<sub>4</sub> nanoparticles produces a form factor that does not have pronounced peaks and therefore leads to a featureless SAXS profile for the nanocomposite (Supporting Information, Figure S7B).

In Figures 3 and 4, the SEM-EDS images of the nanocomposites are shown to evaluate the particle dispersity within the composite through elemental distribution. It is believed that for the syn samples, the particle distribution is

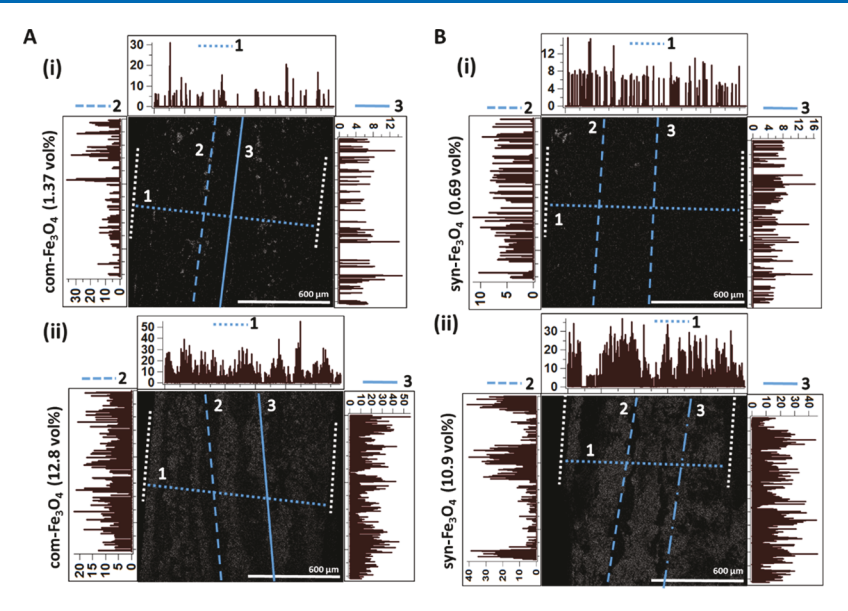


Figure 3. Fe  $K\alpha$  SEM-EDS map and line profile scans of nanocomposite disks in various regions for (A) com-Fe<sub>3</sub>O<sub>4</sub> and (B) syn-Fe<sub>3</sub>O<sub>4</sub>. Dashed white lines at the edges indicate the boundaries of the samples.

random at low concentration, and at higher concentrations, aggregation arises because of magnetic and electrostatic (Hamaker constant) interactions, in accordance with the SAXS results. The magnetic interactions should dominate the interparticle attraction, as reported for Fe<sub>3</sub>O<sub>4</sub> nanoparticles in solution.<sup>64</sup> For the com samples, poor solubility results in nonstatistical distributions. Attempts to analyze individual particle-particle spacing were not made because of available SEM resolution limits, sample thickness, and the inability to obtain high-resolution TEM images of the prepared nanocomposites. In Figures 3 and 4, the EDS-SEM images are shown for the lowest and highest composition com- and syn-Fe<sub>3</sub>O<sub>4</sub> and Ni nanocomposites. Backscattering SEM is available in the Supporting Information (Figure S10). Inspection of the SEM line scans and images reveals that aggregation and sedimentation occur for all types of nanoparticles with increasing volume fraction in the PS composites with the syn samples showing lower aggregation behavior.

A more thorough analysis of the dispersion of Ni in PS can be obtained by imaging the concentration-dependent sedimentation (Figure 4). The com-Ni samples exhibit visible aggregation (striping) at 0.62 vol %, whereas the syn-Ni sample appears to be uniformly dispersed throughout the nanocomposite range studied. Sedimentation within initially cast films is shown in the Supporting Information (Figure S11). Multiple possible arguments can be made for the difference in behavior including surface passivation differences and magnetic moment differences between the samples. For the nanocomposites, it is believed that the observed aggregation differences in com and syn reflect primarily the difference in magnetic moment for the samples, as evidenced by the highest magnetic saturation sample, com-Fe<sub>3</sub>O<sub>4</sub>, exhibiting a higher degree of aggregation than the syn-Fe<sub>3</sub>O<sub>4</sub> sample. This is also evident in the Ni samples where the fcc structure (com) shows more significant aggregation than the hcp (syn) structure reflecting their respective moments.

**Dielectric Properties.** The dielectric properties of the prepared nanocomposites were analyzed by measuring the capacitance of the nanocomposites as a function of frequency to assess the real  $(\varepsilon')$  and imaginary  $(\varepsilon'')$  components of the

complex permittivity.  $^{65,66}$  In Figure 5, the frequency dependence of the real permittivity ( $\varepsilon'$ ) is plotted for the nanocomposites and fits in Figure 6 to the Looyenga model. The imaginary permittivity is shown in the Supporting Information (Figure S12), and the loss tangent is plotted in Figure 7.

Real Permittivity. The real permittivity corresponds to the absorptive or storage ability and is observed to be frequency-dependent, exhibiting a lower dielectric value with increasing frequency and a positive correlation to particle volume fraction in all four nanocomposite systems (Figure 5). The greater increase in the  $\varepsilon'$  for the syn-Ni system versus the com-Ni system can be attributed to the presence of a higher surface passivation level and the polarizable nature of OAm/TOP for syn-Ni. It has been reported that polarizable functional groups respond to electrical fields and enhance the measured  $\varepsilon'$  value at lower frequencies. <sup>67,68</sup> In comparison, pure PS is frequency-independent with a real ( $\varepsilon'$ ) permittivity of 2.45 consistent with reported values (2.4–2.7). <sup>17,33,69</sup>

Earlier nanocomposite studies indicate that the dielectric properties of a nanocomposite can be fit by effective medium theories for well-dispersed nanoparticles in the polymer.<sup>70</sup> This is achieved when the nanoparticle size is on the order of polymer entanglement regime, <sup>34,37</sup> and the surface passivation leads to miscibility between the phases. The developed dielectric models can be subdivided into three categories depending on the degree of material-material, material-host, material-field interactions (group 1 vs group 2) and additional shape and orientation effects (group 3).<sup>73</sup> Dielectric models in group 1 are used for describing the permittivity frequency response for a noninteracting spherical filler in a matrix. We anticipated that for our nanocomposite system that uses spherical nanoparticles below 50 nm in a low-k host polymer matrix with low volume fractions (<0.15), group 1 models would fit the best. When the nanomaterials aggregate in the polymer, the dielectric properties cannot be adequately modeled because of the inhomogeneity of the sample.

Comparison of the fits of the real permittivity data at 1 MHz to the various effective medium models are shown in the Supporting Information (Tables S1 and S2). Inspection of the

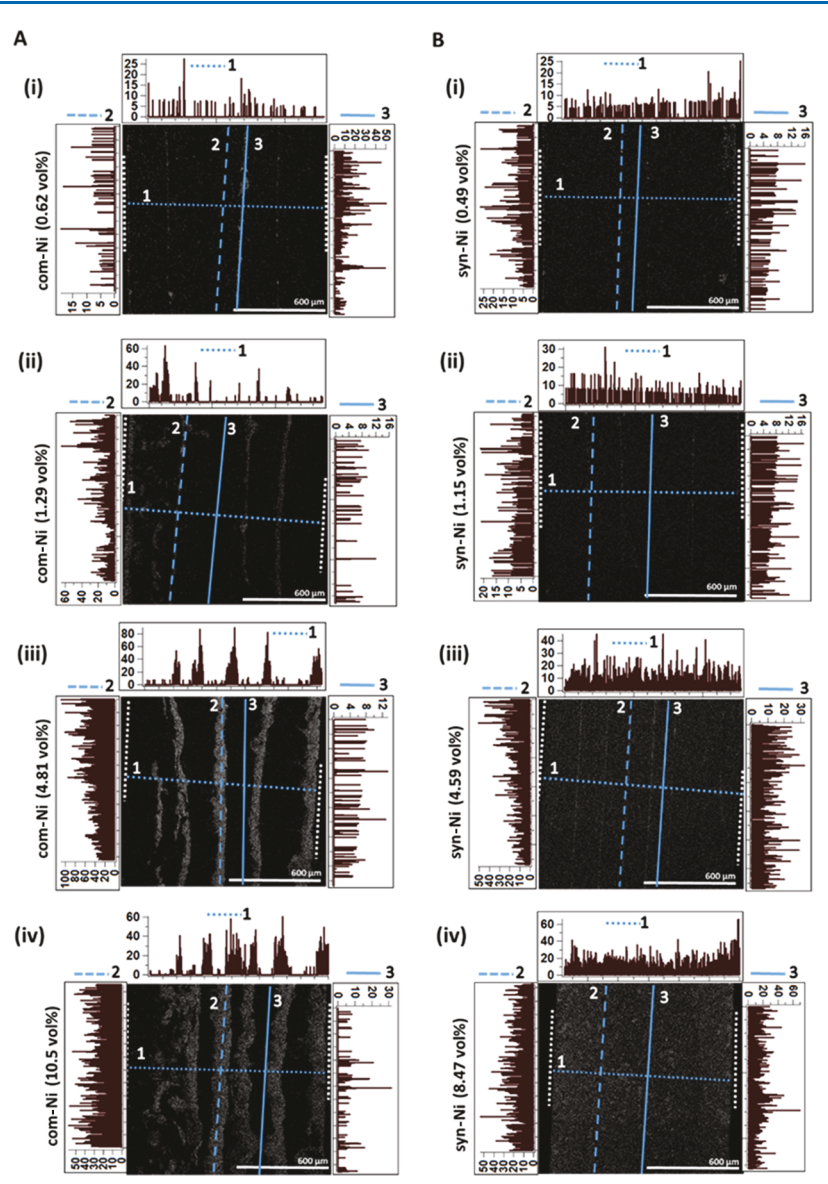


Figure 4. Ni K $\alpha$  SEM-EDS map and line profile scans of pressed nanocomposite samples for all volume fractions of (A) com-Ni and (B) syn-Ni obtained using EDS analysis. Dashed white lines at the edges indicate the boundaries of the samples.

 $\chi^2$  values indicates that the analyzed group 1 and 2 models are within the statistical error. Following from the work of Araújo et al., 73 the Looyenga model is used for further analysis and has the lowest  $\chi^2$  for the tested models. The Looyenga model does not use any geometry assumption (shape or size) of the inclusion in the matrix unlike other dielectric models (almost all group 1 and group 2 models in the Supporting Information (Table S1) including Maxwell-Garnett and Sillars and some group 3 including the Jaysundere-Smith) and uses a "virtual sphere" of a host matrix to which small increments of a second material with different permittivities are added.<sup>75-77</sup> This makes the Looyenga model more applicable to systems where inclusion shape and size might not be the same throughout the host matrix.75-77 Many other effective medium models are based under the assumption of spherical inclusions and/or a certain volume fraction (very low or very high), which limit their application. On the basis of this information, and from the particle distribution of the inclusions seen in the EDS elemental mapping, the Looyenga model was anticipated to be

quite applicable. The real permittivity  $(\varepsilon')$  is fit to the Looyenga effective medium theory, where  $^{75-77}$ 

$$\varepsilon' = ((\varepsilon_{\rm m}')^{1/3}(1 - \nu_{\rm f}) + (\varepsilon_{\rm f}')^{1/3}\nu_{\rm f})^3 \tag{1}$$

where  $\varepsilon'$ ,  $\varepsilon'_{\rm m}$ , and  $\varepsilon'_{\rm f}$  correspond to the real dielectric constant of the composite, matrix, and filler, respectively, and  $v_f$ corresponds to the volume fraction of the nanoparticle. The Looyenga model does not make any shape assumptions for inclusions.  $^{75-77}$  The  $\varepsilon'$  for the nanocomposites is fit to eq 1, as shown in Figure 6. The experimental value for  $v_f = 0.0935$  of the com-Fe<sub>3</sub>O<sub>4</sub> ( $\varepsilon'$  = 2.26) is below pure PS ( $\varepsilon'_{\rm m}$  = 2.45) and is believed to be due to the presence of encapsulated bubbles ( $\varepsilon'$ = 1 for air) lowering the observed dielectric value. As such, it is treated as an outlier but is included in the data set as it is within one standard deviation. Form the fit, the real permittivities for the nanoparticle filler,  $\varepsilon_f$ , are 9.34  $\pm$  1.25 (syn-Ni),  $7.46 \pm 0.78$  (com-Ni),  $4.12 \pm 0.16$  (syn-Fe<sub>3</sub>O<sub>4</sub>), and 5.69  $\pm$  0.65 (com-Fe<sub>3</sub>O<sub>4</sub>). The values of  $\varepsilon'_f$  and  $\chi^2$  for the alternative models (Supporting Information, Table S1) are available in the Supporting Information (Table S2). From the

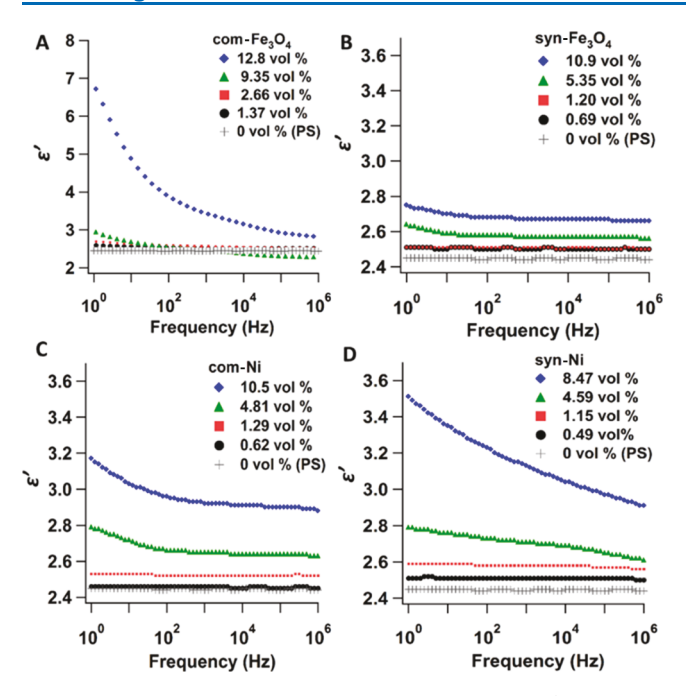


**Figure 5.** Frequency-dependent dielectric measurements (0.1 Hz to 1 MHz) of the real permittivity ( $\varepsilon'$ ) of (A) com-Fe<sub>3</sub>O<sub>4</sub>, (B) syn-Fe<sub>3</sub>O<sub>4</sub>, (C) com-Ni, and (D) syn-Ni nanocomposites at different particle loadings.

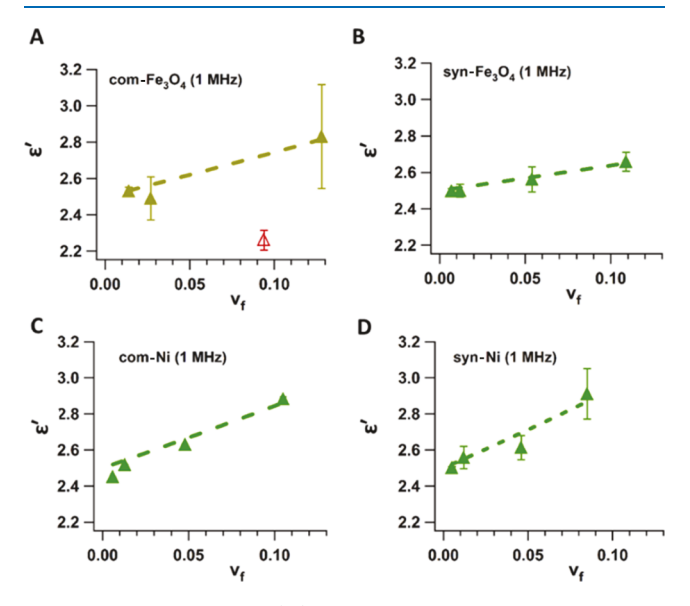


Figure 6. Real permittivity ( $\varepsilon'$ ) of different nanocomposite samples as a function of volume fraction of particles ( $\nu_f$ ). Experimental data are the solid symbols, whereas the dashed lines are fits of the Looyenga model to the data. (A) com-Fe<sub>3</sub>O<sub>4</sub>, (B) syn-Fe<sub>3</sub>O<sub>4</sub>, (C) com-Ni, and (D) syn-Ni nanocomposites.

various other models, only the group 1 and group 2 models give reasonable permittivity values that are close to the Looyenga model results. The group 3 models that include additional variables (see the Supporting Information, Table S1) are unable to fit accurately to the data set for the samples. Most of the group 3 models were developed for interacting high-k fillers loaded at high volume fractions ( $\gg 10\%$ ) and therefore were not expected to model the systems in this work accurately. The larger value for the Ni samples is consistent

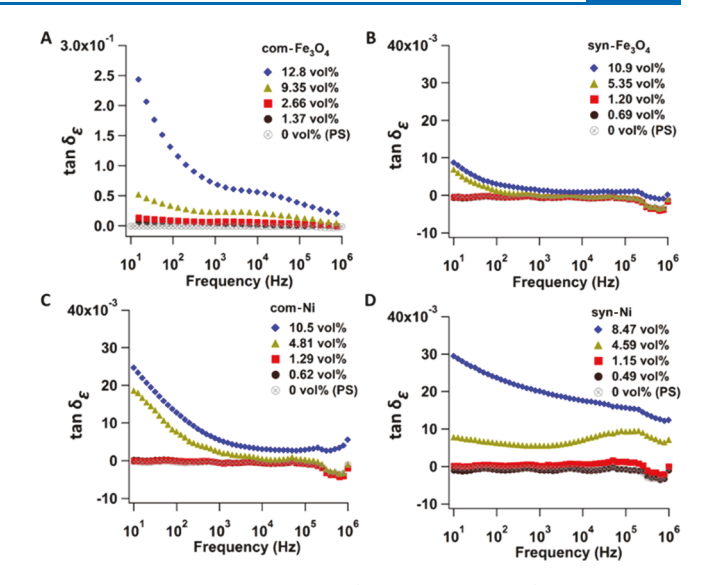


Figure 7. Frequency-dependent (0.1 Hz to 1 MHz) dielectric loss tangent (tan  $\delta_{\varepsilon}$ ) of (A) com-Fe<sub>3</sub>O<sub>4</sub>, (B) syn-Fe<sub>3</sub>O<sub>4</sub>, (C) com-Ni, and (D) syn-Ni nanocomposites.

with the metallic character of Ni and consistent with our early analysis of Ni permittivity.<sup>78</sup>

Imaginary Permittivity. As shown in the Supporting Information (Figure S11), incorporation of synthesized nanoparticles into PS exhibits a linear increase in  $\varepsilon''$  with increasing volume percentage. The imaginary component of the dielectric for PS is negligible, 79 and therefore, any change in  $\varepsilon''$  reflects an increasing contribution from nanoparticle absorptivity. The  $\varepsilon''$  value for increasing volume fraction of com-Ni and com-Fe<sub>3</sub>O<sub>4</sub>, where significant sedimentation is observed, scales nonlinearly and can be empirically fit to a power-law behavior with  $n \approx 2$  (Supporting Information, Figure S13). The empirical fit to the power law is speculated to reflect contributions from the highly polarizable groups present in the PVP surface passivation layer of com-Fe<sub>3</sub>O<sub>4</sub>. In this case, the passivation layer is non-negligible, and therefore, the  $\varepsilon''$ value is anticipated to scale as a surface to volume ratio with increasing volume fraction reflecting the ligand layer and greater interfacial polarization. Further studies are underway to evaluate the passivant-dependent contributions to the dielectric scaling behavior.

Loss Tangent (tan  $\delta$ ). In low-k applications, the  $\varepsilon'$ (imaginary dielectric) is an important parameter; however, the loss tangent (tan  $\delta_{\varepsilon} = \varepsilon''/\varepsilon'$ ) is also critical as the low-k dielectric capacitance influences the performance of the electronic component through heating. The loss tangent, tan  $\delta_{\varepsilon}$ , describes how "lossy" a material is in terms of dissipation of electrical energy. A low loss material has a tan  $\delta_{\varepsilon}$  below 1.  $^{32,80}$ The frequency-dependent loss tangent  $(\varepsilon''/\varepsilon')$  for the nanocomposites is plotted in Figure 7. The nanocomposites are low loss materials over the entire compositional range with the exception of the com-Fe<sub>3</sub>O<sub>4</sub> nanocomposite. Both com samples exhibit the largest frequency sensitivity. At low frequencies, the nanoparticle ligands in the nanocomposite have sufficient time to polarize, which is seen in the upward trend in both  $\varepsilon'$  and  $\varepsilon''$  as the frequency decreases to 0.1 Hz. 33,81 Electrode polarization could also have led to this observed behavior.8

**FDM Filament.** To evaluate potential FDM printing compatibility, printable filament (~2.5 wt % from the TGA

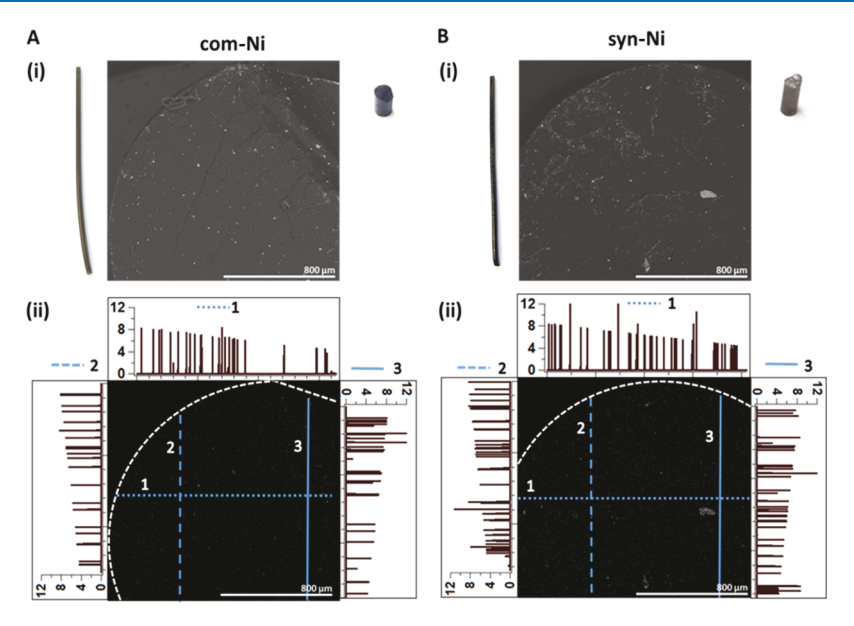


Figure 8. Photographs, BSE images, and EDS mapping of (A) com-Ni and (B) syn-Ni nanocomposite filaments.

analysis of the filament) was produced using the low magnetic syn-Ni and the strongly magnetic com-Ni nanoparticles embedded in PS. The filament is formed using a heated extruder to process the film three times, yielding a fiber ready for printing applications. Although the fiber was not used in the printer, the cross-sectional distribution of Ni in the fiber was analyzed by SEM. As shown in Figure 8, the syn-Ni filament looks black to the eye, whereas the com-Ni filament appears to be a lighter shade, which arises from the better dispersity of syn-Ni versus com-Ni in the polymer. Cross-sectional analysis of the filaments indeed shows that the overall nanoparticle distribution is more homogeneous for syn-Ni than com-Ni in both backscattered electron (BSE) mode and EDS mode. The application of these fibers for FDM printed low-k insulators in electronic architectures is underway.

# CONCLUSIONS

A systematic investigation into the incorporation of well-characterized monodisperse nanoparticles under 50 nm (diameter) of iron oxide and nickel into PS was carried out in this work. The results demonstrate that the PS composite could be a viable candidate for FDM printable materials, when the nanoparticles are uniform. The polymer nanocomposites are observed to be well fit to the Looyenga model up to 50 wt % for well-dispersed syn systems but fail to fit for com systems that tend to aggregate. The agreement to the Looyenga model reflects the high dispersity of nanoparticles in the polymer, as evidenced by the SEM—EDS cross-sectional analysis.

The data from the current study suggest that one can load PS with small monodisperse nanoparticles up to 40-50% wt % ( $\sim 10$  vol %) and still maintain a low-k composite system with low losses even when using a metallic filler such as nickel. This is possible when the materials are well formed and passivated. Unlike certain previous work, our results show that incorporating small nanoparticles that have higher surface area compared to micron fillers did not lead to increased dielectric losses in the nanocomposite even when a metallic nickel filler was used. The dielectric components ( $\varepsilon'$  and  $\varepsilon''$ ) for the nanocomposite decreased with increasing frequency before reaching a constant value excluding the syn-Ni

nanocomposite at the highest volume fraction. As a proof of principle, nanocomposite filaments amenable to FDM printing were produced and shown to maintain their nanoparticle dispersions.

The low loss behavior for the nanocomposites over a wide frequency range for the syn metallic and metal oxide fillers having small sizes and tight size distributions loaded up to physically attainable limits (~50 wt %) was surprising. In comparison to the literature, all the syn materials show better performance. The observation of better performance when synthetically prepared materials with well-defined size, size dispersity, and surface passivated nanoparticles are used as polymer fillers should provide parameters for preparing nanocomposites for FDM printed technologies.

## **■ EXPERIMENTAL SECTION**

**Chemicals.** com iron oxide (com-Fe<sub>3</sub>O<sub>4</sub>) nanopowder 98% (20–30 nm) was purchased from US-Nano and used without further purification. PS 280 kDa, nickel nanopowder (<100 nm, com-Ni) 99%, nickel acetate tetrahydrate (Ni-acac), iron(III) acetylacetonate (Fe-acac), OA, OAm technical grade 70%, 1-octadecene (1-ODE), TOP, *n*-methylpyrrole, toluene, methanol (MeOH), acetone, and chloroform were purchased from Sigma-Aldrich. The materials were used without further purification.

**Synthesis of Nanoparticles.** *syn Iron Oxide* (syn- $Fe_3O_4$ ). Spherical magnetite ( $11 \pm 0.9$  nm) nanoparticles passivated by OA/OAm were synthesized by following a previously established route. In brief, 500 mg (0.00142 mol) of Feacac was dissolved in 18 mL (0.0547 mol) of OAm and 20 mL (0.0628 mol) of OAc. The solution was heated to 180 °C, and 2 mL (0.0225 mol) of n-methylpyrrole was rapidly injected. The temperature was held at 180 °C for 30 min and then cooled to room temperature. To isolate  $Fe_3O_4$  from the reaction mixture, MeOH was added until the solution became opaque, and the resultant nanoparticles were removed by applying a magnetic field. The magnetically separated  $Fe_3O_4$  nanoparticles were redispersed in toluene, reprecipitated by the addition of MeOH, and dried under vacuum.

syn Nickel Nanoparticles (syn-NiNPs). Spherical hcp-Ni (20 nm) nanoparticles, passivated by TOP, were prepared by combining 3.0 g (0.012 mol) of nickel acetate, 72 mL (0.23 mol) of 1-ODE, and 12 mL (0.036 mol) of OAm added to a 250 mL round-bottom flask. The solution was degassed under vacuum at 110 °C until no gas evolution was observed and back-filled with N<sub>2</sub>. To the solution, 5.4 mL (0.012 mol) of TOP was added, and the temperature of contents increased to 245 °C. NiNPs were observed to begin forming in solution at 200 °C as observed by the solution color turning black. When the temperature reached 245 °C, the contents were removed from the heating mantle and immediately cooled to room temperature. The reaction was poured into a centrifuge tube, and the nickel nanoparticles were precipitated by the addition of 10 mL toluene, followed by 30 mL of MeOH. The resulting solution was centrifuged for 5 min. After removing the supernatant, the pellet was redispersed in toluene. To precipitate the NiNPs, excess MeOH was added, followed by isolation through centrifugation before drying under vacuum.

Nanoparticle-PS Composites. The nanoparticle-polymer composites were prepared with particle loadings between 0 and 15 vol % (Table 1) by blending chloroform dispersed PS and nanoparticles dispersed in chloroform with the assistance of sonication at 40 °C. The polymer composite is formed by slow solvent evaporation to form a viscous solution, cast onto a flat glass surface to form a film, and then further dried under vacuum for 24 h. To minimize bubble formation in the cured nanopolymer composite film during the vacuum drying step, a multistep drying procedure is followed, wherein initially the sample is heated using an oven from 25 to 80 °C (10 °C/h) over 6 h, held at 80 °C for 12 h, followed by vacuum drying at 110 °C for 12 h to fully cure the polymer composite. To ensure adequate material for dielectric measurements and cross-sectional analysis by SEM imaging, an 8 mm × 1 mm disk is formed from the above nanoparticle-polymer film by punching 5/16th in. disks from the polymer composite, stacking four disks, and hot pressing in an aluminum mold at 185 °C at a force of 15 000 pounds for 10 min.

**Filament Formation.** A low volume fraction printable filament for the syn-Ni and com-Ni samples was prepared by extruding precast and dried nanocomposite films using a Filabot EX2 Filament Extruder operating at 220 °C. The extruded filament was broken up and extruded 3 times to improve homogeneity.

**Transmission Electron Microscopy.** Nanoparticle samples were drop-cast, from toluene dispersion, onto 300 mesh carbon-coated copper grids and left to dry under vacuum overnight. The TEM images were recorded using a JEM-ARM200cF electron microscope at a 200 kV acceleration voltage.

Scanning Electron Microscopy. SEM-EDS imaging analysis of cross sections of the composite cast film, pressed disks and extruded filament was performed on cleaved samples mounted onto a carbon tape and placed on 45°/90° (Ted Pella 16104) low profile aluminum mount to allow cross-sectional imaging. The mounted samples were carbon-coated (4 nm) using a Balzers Mini deposition system MED 010 prior to SEM imaging to prevent charging. SEM imaging was performed on a FEI Nova NanoSEM 400 operating at 20 kV with a spot size of 4.0. The images were collected with an Everhart—Thornley detector (ETD), a BSE detector, or an Oxford INCA X-Sight EDS detector. The BSE mode and EDS mapping were used to

identify the dispersion of nanoparticles within the polymer for the lowest and highest volume fractions of nanoparticles.

Thermogravimetric Analysis. TGA was performed on a TA Instruments Q50 thermogravimetric analyzer. The samples were heated at a rate of 10 °C/min from room temperature to 100 °C and held for 5 min before continuing to ramp at 10 °C/min to 550 °C. Measurements were performed under nitrogen to prevent further oxidation.

**Magnetic Measurements.** Magnetic properties were studied with a superconducting quantum interference device (SQUID) magnetometer, MPMS-XL (Quantum Design). Field-dependent magnetization was measured at 300 K, with the applied field varying from 0 to 1 T and back.

**Differential Scanning Calorimetry (DSC).** Measurements were carried out at the highest loading levels for the nanocomposite using a TA Q250 calorimeter. The samples were subjected to a heat/cool/heat experimental procedure: ramp at 10 °C/min to 300.00 °C; ramp at 10 °C/min to 50.00 °C; and ramp at 10 °C/min to 300.00 °C.

**Dielectric Spectroscopy.** The dielectric spectroscopy was performed on the composite disks (8 mm × 1 mm) on a Novocontrol impedance dielectric spectrometer (Rohde & Schwarz ZVA), and a parallel-plate geometry and an Alpha-A modular analyzer were utilized to calculate the capacitance and conductivity of each sample. WinDETA software provided the calibration protocols and experimentation setup. The measurements were taken at 1.5 V, for each frequency, and averaged three times for each data point. Measurements were taken over 10 Hz steps over the frequency range chosen.

**Powder X-ray Diffraction.** The pXRD patterns for Ni nanoparticles and for all volume percent nanocomposites were acquired on a Rigaku Ultima III diffractometer equipped with a Cu K $\alpha$  source. Because of the presence of Fe fluorescence, the Fe<sub>3</sub>O<sub>4</sub> composites were analyzed on a PANalyticial X'pert Pro (Cu K $\alpha$  source with a filter for the removal of iron fluorescence). Data were collected at room temperature in the  $2\theta$  range of  $10-80^\circ$ .

**Small-Angle X-ray Scattering.** SAXS measurements were performed between 0.1 and  $3.7^{\circ}$   $(2\theta)$  in transmission mode on 8 mm  $\times$  1 mm disks of the nanocomposite using a Bruker Nanostar instrument with a Cu K $\alpha$  source ( $\lambda$  = 0.154 nm). The sample was placed in an aluminum sample holder. Intensity versus scattering vector (q) plots, where  $q = 4\pi/\lambda \sin(\theta)$ , were generated by integrating over a 1 mm  $\times$  1 mm area of the detector (600 s averaging time).

#### ASSOCIATED CONTENT

#### S Supporting Information

The Supporting Information is available free of charge on the ACS Publications website at DOI: 10.1021/acsomega.8b01477.

Additional pXRD, TGA, SQUID, DSC, SAXS, SEM, dielectric spectroscopy, and dielectric model fitting results for nanoparticles and nanocomposites (PDF)

# AUTHOR INFORMATION

## **Corresponding Authors**

\*E-mail: sramakrishnan@fsu.edu (S.R.). \*E-mail: strouse@chem.fsu.edu (G.F.S.).

ORCID ®

Geoffrey F. Strouse: 0000-0003-0841-282X

#### Notes

The authors declare no competing financial interest.

# ACKNOWLEDGMENTS

G.F.S., D.A.H and P.N.V. wish to thank the National Science Foundation (NSF CHE-1608364) for funding. F.M. and S.R. were supported by AMSRD-ARLRO-SI proposal # 62885-MS-REP (W911NF-13-1-0132) from the Department of Defense (Army Research Office). Partial support for the work was also provided by the NSF award # 1735968 (CREST Center for Complex Materials Design for Multidimensional Additive Processing—CoManD). The authors would like to acknowledge the Army Research Lab (Aberdeen Proving Grounds, MD) for the use of the Novocontrol-Dielectric Spectrometer in the dielectric studies and Oak Ridge Associated Universities for financial support. F.M. would also like to acknowledge the support from the SMART fellowship. A portion of this work (TEM Imaging) was performed at the National High Magnetic Field Laboratory, which is supported by National Science Foundation Cooperative Agreement # DMR-1157490 and the State of Florida.

### REFERENCES

- (1) Balazs, A. C.; Emrick, T.; Russell, T. P. Nanoparticle Polymer Composites: Where Two Small Worlds Meet. *Science* **2006**, *314*, 1107–1110.
- (2) Hussain, F.; Hojjati, M.; Okamoto, M.; Gorga, R. E. Review Article: Polymer-Matrix Nanocomposites, Processing, Manufacturing, and Application: An Overview. *J. Compos. Mater.* **2006**, *40*, 1511–1575.
- (3) Marquis, D. M.; Guillaume, E.; Chivas-Joly, C. Properties of Nanofillers in Polymer. *Nanocomposites and Polymers with Analytical Methods*; InTech, 2011.
- (4) Šupová, M.; Martynková, G. S.; Barabaszová, K. Effect of Nanofillers Dispersion in Polymer Matrices: A Review. *Sci. Adv. Mater.* **2011**, *3*, 1–25.
- (5) Vaia, R. A.; Maguire, J. F. Polymer Nanocomposites with Prescribed Morphology: Going beyond Nanoparticle-Filled Polymers. *Chem. Mater.* **2007**, *19*, 2736–2751.
- (6) Li, S.; Lin, M. M.; Toprak, M. S.; Kim, D. K.; Muhammed, M. Nanocomposites of Polymer and Inorganic Nanoparticles for Optical and Magnetic Applications. *Nano Rev* **2010**, *1*, 5214.
- (7) Imai, Y. Inorganic Nano-Fillers for Polymers. *Encyclopedia of Polymeric Nanomaterials*; Springer, 2014; Vols. 1–7.
- (8) Ramajo, L. A.; Cristóbal, A. A.; Botta, P. M.; Porto López, J. M.; Reboredo, M. M.; Castro, M. S. Dielectric and Magnetic Response of Fe3O4/Epoxy Composites. *Compos. Part A Appl. Sci. Manuf.* **2009**, 40, 388–393.
- (9) Lee, H. S.; Lee, A. S.; Baek, K.-Y.; Hwang, S. S. Low Dielectric Materials for Microelectronics, 1st ed; Intech Open Limited, 2012; pp 69–76.
- (10) Vengatesan, M. R.; Devaraju, S.; Dinakaran, K.; Alagar, M. SBA-15 Filled Polybenzoxazine Nanocomposites for Low-k Dielectric Applications. *J. Mater. Chem.* **2012**, *22*, 7559.
- (11) Hatton, B. D.; Landskron, K.; Hunks, W. J.; Bennett, M. R.; Shukaris, D.; Perovic, D. D.; Ozin, G. A. Materials Chemistry for Low-k Materials. *Mater. Today* **2006**, *9*, 22–31.
- (12) Lis, M.; Plaut, M.; Zai, A.; Cipolle, D.; Russo, J.; Fedynyshyn, T. High Performance, 3D-Printable Dielectric Nanocomposites for Millimeter Wave Devices. ACS Appl. Mater. Interfaces 2016, 8, 34019–34026.
- (13) Farrell, R.; Goshal, T.; Cvelbar, U.; Petkov, N.; Morris, M. A. Advances in Ultra Low Dielectric Constant Ordered Porous Materials. *Electrochem. Soc. Interface* **2011**, *20*, 39–46.
- (14) Lee, H. S.; Lee, A. S.; Baek, K.-Y.; Hwang, S. S. Dielectric Materials; InTech, 2012.

(15) Treichel, H.; Ruhl, G.; Ansmann, P.; Würl, R.; Müller, C.; Dietlmeier, M. Low dielectric constant materials for interlayer dielectric. *Microelectron. Eng.* **1998**, *40*, 1–19.

- (16) Shamiryan, D.; Abell, T.; Iacopi, F.; Maex, K. Low-k Dielectric Materials. *Mater. Today* **2004**, *7*, 34–39.
- (17) Barber, P.; Balasubramanian, S.; Anguchamy, Y.; Gong, S.; Wibowo, A.; Gao, H.; Ploehn, H. J.; Loye, H.-C. z. Polymer Composite and Nanocomposite Dielectric Materials for Pulse Power Energy Storage. *Materials* **2009**, *2*, 1697–1733.
- (18) Tanaka, T.; Montanari, G. C.; Mulhaupt, R. Polymer Nanocomposites as Dielectrics and Electrical Insulation-Perspectives for Processing Technologies, Material Characterization and Future Applications. *IEEE Trans. Dielectr. Electr. Insul.* **2004**, *11*, 763–784.
- (19) Khan, S.; Lorenzelli, L.; Dahiya, R. S. Technologies for Printing Sensors and Electronics Over Large Flexible Substrates: A Review. *IEEE Sens. J.* **2015**, *15*, 3164–3185.
- (20) Sarobol, P.; Cook, A.; Clem, P. G.; Keicher, D.; Hirschfeld, D.; Hall, A. C.; Bell, N. S. Additive Manufacturing of Hybrid Circuits. *Annu. Rev. Mater. Res.* **2016**, *46*, 41–62.
- (21) Postiglione, G.; Natale, G.; Griffini, G.; Levi, M.; Turri, S. Conductive 3D Microstructures by Direct 3D Printing of Polymer/Carbon Nanotube Nanocomposites via Liquid Deposition Modeling. *Compos. Part A Appl. Sci. Manuf.* **2015**, *76*, 110–114.
- (22) Wu, S.-Y.; Yang, C.; Hsu, W.; Lin, L. 3D-Printed Microelectronics for Integrated Circuitry and Passive Wireless Sensors. *Microsystems Nanoeng.* **2015**, *1*, 15013.
- (23) Shemelya, C.; Banuelos-Chacon, L.; Melendez, A.; Kief, C.; Espalin, D.; Wicker, R.; Krijnen, G.; MacDonald, E. Multi-Functional 3D Printed and Embedded Sensors for Satellite Qualification Structures. In *Sensors*, 2015 IEEE; IEEE, 2015; pp 1–4.
- (24) Kamyshny, A.; Magdassi, S. Conductive Nanomaterials for Printed Electronics. *Small* **2014**, *10*, 3515–3535.
- (25) Panda, M.; Srinivas, V.; Thakur, A. K. On the Question of Percolation Threshold in Polyvinylidene Fluoride/Nanocrystalline Nickel Composites. *Appl. Phys. Lett.* **2008**, *92*, 132905.
- (26) do Nascimento, E.; Ramos, A.; Windmoller, D.; Reig Rodrigo, P.; Teruel Juanes, R.; Ribes Greus, A.; Amigó Borrás, V.; Coelho, L. A. F. Breakdown, Free-Volume and Dielectric Behavior of the Nanodielectric Coatings Based on Epoxy/Metal Oxides. *J. Mater. Sci. Mater. Electron.* **2016**, *27*, 9240–9254.
- (27) Toor, A.; So, H.; Pisano, A. P. Improved Dielectric Properties of Polyvinylidene Fluoride Nanocomposite Embedded with Poly-(Vinylpyrrolidone)-Coated Gold Nanoparticles. *ACS Appl. Mater. Interfaces* **2017**, *9*, 6369–6375.
- (28) Fillery, S. P.; Koerner, H.; Drummy, L.; Dunkerley, E.; Durstock, M. F.; Schmidt, D. F.; Vaia, R. A. Nanolaminates: Increasing Dielectric Breakdown Strength of Composites. *ACS Appl. Mater. Interfaces* **2012**, *4*, 1388–1396.
- (29) Paul, D. R.; Robeson, L. M. Polymer Nanotechnology: Nanocomposites. *Polymer* **2008**, *49*, 3187–3204.
- (30) Hu, P.; Shen, Y.; Guan, Y.; Zhang, X.; Lin, Y.; Zhang, Q.; Nan, C.-W. Topological-Structure Modulated Polymer Nanocomposites Exhibiting Highly Enhanced Dielectric Strength and Energy Density. *Adv. Funct. Mater.* **2014**, 24, 3172–3178.
- (31) Idris, F. M.; Hashim, M.; Abbas, Z.; Ismail, I.; Nazlan, R.; Ibrahim, I. R. Recent Developments of Smart Electromagnetic Absorbers Based Polymer-Composites at Gigahertz Frequencies. *J. Magn. Magn. Mater.* **2016**, *405*, 197–208.
- (32) Xu, J.; Wong, C. P. Low-Loss Percolative Dielectric Composite. *Appl. Phys. Lett.* **2005**, *87*, 082907.
- (33) Zhang, L.; Chen, S.; Yuan, S.; Wang, D.; Hu, P.-H.; Dang, Z.-M. Low Dielectric Loss and Weak Frequency Dependence of Dielectric Permittivity of the CeO2/Polystyrene Nanocomposite Films. *Appl. Phys. Lett.* **2014**, *105*, 052905.
- (34) Roy, M.; Nelson, J. K.; MacCrone, R. K.; Schadler, L. S.; Reed, C. W.; Keefe, R.; Zenger, W. Polymer nanocomposite dielectrics—the role of the interface. *IEEE Trans. Dielectr. Electr. Insul.* **2005**, *12*, 629–643.

(35) Tanaka, T. Dielectric Nanocomposites with Insulating Properties. *IEEE Trans. Dielectr. Electr. Insul.* **2005**, 12, 914–928.

- (36) Cho, S.-D.; Lee, S.-Y.; Hyun, J.-G.; Paik, K.-W. Comparison of theoretical predictions and experimental values of the dielectric constant of epoxy/BaTiO3 composite embedded capacitor films. *J. Mater. Sci. Mater. Electron.* **2005**, *16*, 77–84.
- (37) Polizos, G.; Tuncer, E.; Tomer, V.; Sauers, I.; Randall, C. A.; Manias, E. Dielectric Spectroscopy of Polymer-Based Nanocomposite Dielectrics with Tailored Interfaces and Structured Spatial Distribution of Fillers. In *Nanoscale Spectroscopy with Applications*; CRC Press, 2013; pp 93–130.
- (38) Psarras, G. C.; Manolakaki, E.; Tsangaris, G. M. Dielectric dispersion and ac conductivity in-Iron particles loaded-polymer composites. *Compos. Part A Appl. Sci. Manuf.* **2003**, 34, 1187–1198.
- (39) Wang, X.; Li, W.; Luo, L.; Fang, Z.; Zhang, J.; Zhu, Y. High Dielectric Constant and Superparamagnetic Polymer-Based Nanocomposites Induced by Percolation Effect. *J. Appl. Polym. Sci.* **2012**, 125, 2711–2715.
- (40) Ren, L.; Zhao, J.; Wang, S.-J.; Zha, J.-W.; Hu, G.-H.; Dang, Z.-M. Remarkably Variable Dielectric and Magnetic Properties of Poly(Vinylidene Fluoride) Nanocomposite Films with Triple-Layer Structure. *Compos. Sci. Technol.* **2015**, *107*, 107–112.
- (41) Pissis, P.; Fragiadakis, D.; Kanapitsas, A.; Delides, K. Broadband Dielectric Relaxation Spectroscopy in Polymer Nanocomposites. *Macromol. Symp.* **2008**, 265, 12–20.
- (42) Wang, M.; Pan, N. Predictions of Effective Physical Properties of Complex Multiphase Materials. *Mater. Sci. Eng. R Reports* **2008**, 63, 1–30.
- (43) Jayasundere, N.; Smith, B. V. Dielectric constant for binary piezoelectric 0-3 composites. J. Appl. Phys. 1993, 73, 2462–2466.
- (44) Vladimír, H.; Karel, L. New Mixing Rule of Polymer Composite Systems. WSEAS Trans. Electron. **2010**, *9*, 381–384.
- (45) Todd, M. G.; Shi, F. G. Complex Permittivity of Composite Systems: A Comprehensive Interphase Approach. *IEEE Trans. Dielectr. Electr. Insul.* **2005**, *12*, 601–611.
- (46) Ajayan, P. M.; Schadler, L. S.; Braun, P. V. Nanocomposite Science and Technology; John Wiley & Sons, 2006; pp 1–229.
- (47) Liu, C.; Zhang, Z. J. Size-Dependent Superparamagnetic Properties of Mn Spinel Ferrite Nanoparticles Synthesized from Reverse Micelles. *Chem. Mater.* **2001**, *13*, 2092–2096.
- (48) Jun, Y.-w.; Seo, J.-w.; Cheon, J. Nanoscaling Laws of Magnetic Nanoparticles and Their Applicabilities in Biomedical Sciences. *Acc. Chem. Res.* **2008**, *41*, 179–189.
- (49) Baumgartner, J.; Bertinetti, L.; Widdrat, M.; Hirt, A. M.; Faivre, D. Formation of Magnetite Nanoparticles at Low Temperature: From Superparamagnetic to Stable Single Domain Particles. *PLoS One* **2013**, *8*, No. e57070.
- (50) Xuan, S.; Wang, Y.-X. J.; Yu, J. C.; Cham-Fai Leung, K. Tuning the Grain Size and Particle Size of Superparamagnetic Fe3O4 Microparticles. *Chem. Mater.* **2009**, *21*, 5079–5087.
- (51) He, X.; Zhong, W.; Au, C.-T.; Du, Y. Size Dependence of the Magnetic Properties of Ni Nanoparticles Prepared by Thermal Decomposition Method. *Nanoscale Res. Lett.* **2013**, *8*, 446.
- (52) Chandran, S.; Basu, J. K.; Mukhopadhyay, M. K. Variation in Glass Transition Temperature of Polymer Nanocomposite Films Driven by Morphological Transitions. *J. Chem. Phys.* **2013**, *138*, 014902.
- (53) Ash, B. J.; Siegel, R. W.; Schadler, L. S. Glass-transition temperature behavior of alumina/PMMA nanocomposites. *J. Polym. Sci. Part B Polym. Phys.* **2004**, 42, 4371–4383.
- (54) Schadler, L. S.; Kumar, S. K.; Benicewicz, B. C.; Lewis, S. L.; Harton, S. E. Designed Interfaces in Polymer Nanocomposites: A Fundamental Viewpoint. *MRS Bull.* **2007**, *32*, 335–340.
- (55) Hanemann, T.; Szabó, D. V. Polymer-Nanoparticle Composites: From Synthesis to Modern Applications. *Materials* **2010**, *3*, 3468–3517.
- (56) Mbhele, Z. H.; Salemane, M. G.; van Sittert, C. G. C. E.; Nedeljković, J. M.; Djoković, V.; Luyt, A. S. Fabrication and

Characterization of Silver-Polyvinyl Alcohol Nanocomposites. *Chem. Mater.* **2003**, *15*, 5019-5024.

- (57) Lebedev, S. M.; Gefle, O. S.; Tkachenko, S. N. Metal-Polymer PVDF/Nickel Composites and Evaluation of Their Dielectric and Thermal Properties. *J. Electrostat.* **2010**, *68*, 122–127.
- (58) Li, T.; Senesi, A. J.; Lee, B. Small Angle X-ray Scattering for Nanoparticle Research. *Chem. Rev.* **2016**, *116*, 11128–11180.
- (59) Lan, Q.; Francis, L. F.; Bates, F. S. Silica Nanoparticle Dispersions in Homopolymer versus Block Copolymer. *J. Polym. Sci. Part B Polym. Phys.* **2007**, 45, 2284–2299.
- (60) Kisner, A. Ultrathin Gold Nanowires: Chemistry, Electrical Characterization and Application to Sense Cellular Biology. Ph.D. Thesis, RWTH Aachen University, July 2013.
- (61) Wang, Z.; Wen, X.-D.; Hoffmann, R.; Son, J. S.; Li, R.; Fang, C.-C.; Smilgies, D.-M.; Hyeon, T. Reconstructing a Solid-Solid Phase Transformation Pathway in CdSe Nanosheets with Associated Soft Ligands. *Proc. Natl. Acad. Sci. U.S.A.* **2010**, *107*, 17119–17124.
- (62) Garland, E. R.; Rosen, E. P.; Clarke, L. I.; Baer, T. Structure of Submonolayer Oleic Acid Coverages on Inorganic Aerosol Particles: Evidence of Island Formation. *Phys. Chem. Chem. Phys.* **2008**, *10*, 3156–3161.
- (63) Wang, D.; Lin, B.; Shen, T.; Wu, J.; Hao, F.; Xia, C.; Gong, Q.; Tang, H.; Song, B.; Ai, H. Control of the Interparticle Spacing in Superparamagnetic Iron Oxide Nanoparticle Clusters by Surface Ligand Engineering. *Chin. Phys. B* **2016**, 25, 077504.
- (64) Kohl, P. A. Low-Dielectric Constant Insulators for Future Integrated Circuits and Packages. *Annu. Rev. Chem. Biomol. Eng.* **2011**, 2, 379–401.
- (65) Wolter, F.; Thom, F. A Parallel-Plate Capacitor Used to Determine the Complex Permittivity of Supercooled Aqueous Solutions in the 1 MHz Range. *Meas. Sci. Technol.* **1996**, *7*, 969–975.
- (66) Grove, T. T.; Masters, M. F.; Miers, R. E. Determining Dielectric Constants Using a Parallel Plate Capacitor. *Am. J. Phys.* **2005**, 73, 52–56.
- (67) Mantese, J. V.; Micheli, A. L.; Dungan, D. F.; Geyer, R. G.; Baker-Jarvis, J.; Grosvenor, J. Applicability of effective medium theory to ferroelectric/ferrimagnetic composites with composition and frequency-dependent complex permittivities and permeabilities. *J. Appl. Phys.* **1996**, *79*, 1655–1660.
- (68) Dong, X. L.; Zhang, X. F.; Huang, H.; Zuo, F. Enhanced Microwave Absorption in Ni/Polyaniline Nanocomposites by Dual Dielectric Relaxations. *Appl. Phys. Lett.* **2008**, *92*, 013127.
- (69) Crippa, M.; Bianchi, A.; Cristofori, D.; D'Arienzo, M.; Merletti, F.; Morazzoni, F.; Scotti, R.; Simonutti, R. High dielectric constant rutile-polystyrene composite with enhanced percolative threshold. *J. Mater. Chem. C* **2013**, *1*, 484–492.
- (70) Reynolds, J. A.; Hough, J. M. Formulae for Dielectric Constant of Mixtures. *Proc. Phys. Soc. Sect. B* **1957**, *70*, 769–775.
- (71) Sihvola, A. H.; Kong, J. A. Effective Permittivity of Dielectric Mixtures. *IEEE Trans. Geosci. Remote Sens.* **1988**, 26, 420–429.
- (72) Carpi, F.; De Rossi, D. Improvement of Electromechanical Actuating Performances of a Silicone Dielectric Elastomer by Dispersion of Titanium Dioxide Powder. *IEEE Trans. Dielectr. Electr. Insul.* **2005**, *12*, 835–843.
- (73) Araújo, M. C.; Costa, C. M.; Lanceros-Méndez, S. Evaluation of Dielectric Models for Ceramic/Polymer Composites: Effect of Filler Size and Concentration. *J. Non. Cryst. Solids* **2014**, *387*, 6–15.
- (74) Ezzat, M.; Sabiha, N. A.; Izzularab, M. Accurate Model for Computing Dielectric Constant of Dielectric Nanocomposites. *Appl. Nanosci.* **2014**, *4*, 331–338.
- (75) Dube, D. C. Study of Landau-Lifshitz-Looyenga's Formula for Dielectric Correlation between Powder and Bulk. *J. Phys. D. Appl. Phys.* **1970**, 3, 1648.
- (76) Tuncer, E. The Landau-Lifshitz/Looyenga Dielectric Mixture Expression and Its Self-Similar Fractal Nature. **2005**, arXiv:cond-mat/0503750.
- (77) Scheller, M.; Jansen, C.; Koch, M. Applications of Effective Medium Theories in the Terahertz Regime. In *Recent Optical and Photonic Technologies*; InTech, 2010.

(78) Ashley, B.; Vakil, P. N.; Lynch, B. B.; Dyer, C. M.; Tracy, J. B.; Owens, J.; Strouse, G. F. Microwave Enhancement of Autocatalytic Growth of Nanometals. *ACS Nano* **2017**, *11*, 9957–9967.

- (79) Goyal, R. K.; Jagadale, P. A.; Mulik, U. P. Thermal, Mechanical, and Dielectric Properties of Polystyrene/Expanded Graphite Nanocomposites. *J. Appl. Polym. Sci.* **2009**, *111*, 2071–2077.
- (80) Jonscher, A. K. Low-Loss Dielectrics. J. Mater. Sci. 1999, 34, 3071-3082.
- (81) Hyuga, M.; Tanaka, T.; Ohki, Y.; Imai, T.; Harada, M.; Ochi, M. Correlation between Mechanical and Dielectric Relaxation Processes in Epoxy Resin Composites with Nano-and Micro-Fillers. *IEEJ Trans. Fundam. Mater.* **2011**, *131*, 1041–1047.
- (82) Chanmal, C. V.; Jog, J. P. Dielectric relaxations in PVDF/BaTiO3 nanocomposites. *Express Polym Lett* **2008**, *2*, 294–301.
- (83) Tan, Y.; Zhuang, Z.; Peng, Q.; Li, Y. Room-Temperature Soft Magnetic Iron Oxide Nanocrystals: Synthesis, Characterization, and Size-Dependent Magnetic Properties. *Chem. Mater.* **2008**, *20*, 5029–5034.